Single-cell genotyping and transcriptomic profiling in focal cortical dysplasia

Stephanie Baulac

stephanie.baulac@icm-institute.org

Institut du Cerveau (ICM) https://orcid.org/0000-0001-6430-4693

Sara Baldassari

Paris Brain Institute

Esther Klingler

University of Geneva

Lucia Gomez Teijeiro

University of Geneva

Marion Doladilhe

Institut du Cerveau

Corentin Raoux

Institut du Cerveau (ICM)

Sergi Roig-Puiggros

University of Geneva https://orcid.org/0000-0001-5909-218X

Sara Bizzotto

Sorbonne University, Paris Brain Institute (ICM)

Lina Sami

Institut du Cerveau (ICM)

Theo Ribierre

Institut du Cerveau https://orcid.org/0000-0002-5003-0991

Eleonora Aronica

Amsterdam UMC https://orcid.org/0000-0002-3542-3770

Homa Adle-Biassette

Lariboisière Hospital

Mathilde Chipaux

Fondation Ophtalmologique Adolphe de Rothschild

Denis Jabaudon

University of Geneva https://orcid.org/0000-0003-2438-4769

Article

Keywords:

Posted Date: March 15th, 2024

DOI: https://doi.org/10.21203/rs.3.rs-4014535/v1

Additional Declarations:
There is **NO** Competing Interest.

Supplementary Tables are not available with this version

Single-cell genotyping and transcriptomic profiling in focal cortical dysplasia

Sara Baldassari*[1], Esther Klingler*[2,3,4,5], Lucia Gomez Teijeiro[5], Marion Doladilhe[1], Corentin Raoux[1], Sergi Roig Puiggros[5], Sara Bizzotto[1], Lina Sami[1], Théo Ribierre[1,5,6], Eleonora Aronica[7,8], Homa Adle-Biassette[9,10], Mathilde Chipaux[11], Denis Jabaudon[5,12] and Stéphanie Baulac[1]

1. Institut du Cerveau-Paris Brain Institute-ICM, Sorbonne Université, Inserm, CNRS, Hôpital de la Pitié Salpêtrière, F-75013 Paris, France.
2. VIB-KU Leuven Center for Brain & Disease Research, 3000 Leuven, Belgium
3. KU Leuven, Department of Neurosciences, Leuven Brain Institute, 3000 Leuven, Belgium
4. KU Leuven Institute for Single Cell Omics, 3000 Leuven, Belgium
5. Department of Basic Neurosciences, University of Geneva, 1211 Geneva, Switzerland.
6. Fondation Campus Biotech Geneva, Geneva, Switzerland
7. Amsterdam UMC, University of Amsterdam, Amsterdam Neuroscience, Department of (Neuro)Pathology, Amsterdam, The Netherlands
8. Stichting Epilepsie Instellingen Nederland (SEIN), Heemstede, The Netherlands
9. Université Paris Cité, Inserm, NeuroDiderot, F-75019 Paris, France
10. Department of Pathology, AP-HP, Lariboisière hospital, 75010 Paris, France
11. Department of Pediatric Neurosurgery, Rothschild Foundation Hospital EpiCARE, 75019, Paris, France
12. Clinic of Neurology, Geneva University Hospital, 1211 Geneva, Switzerland.

* These authors contributed equally

Corresponding author: Stéphanie Baulac; Institut du Cerveau, 47 bd de l'hôpital, 75013, Paris, France; stephanie.baulac@icm-institute.org

Competing interests

The authors have declared that no conflict of interest exists.

ABSTRACT

Focal cortical dysplasia type II (FCDII) is a cortical malformation causing refractory epilepsy. FCDII arises from developmental somatic mutations in mTOR pathway genes, leading to focal cortical dyslamination and abnormal cytomegalic cells. Which cell types carry pathogenic mutations and how they affect cell-type-specific transcriptional programs remains unknown. To address this question, here we combined single-nucleus genotyping and transcriptomics in morphologically-identified cells using surgical cortical samples from genetically-characterized FCDII patients. Mutations were predominantly detected in glutamatergic neurons and astrocytes and only a small fraction of mutated cells exhibited cytomegalic features, revealing incomplete penetrance of FCDII-causing mutations. Moreover, we identified cell-type-specific transcriptional dysregulations in both mutated and non-mutated FCDII cells, including synapse and neurodevelopment-related pathways, that may account for epilepsy, and dysregulation of mitochondrial metabolism pathways in cytomegalic cells. Together, these findings reveal cell-autonomous and non-cell-autonomous mechanisms at play in FCDII, towards the development of precision therapies for this disorder.

INTRODUCTION

All cells of the body derive from a single dividing fertilized egg, yet daughter cells have different genomes due to somatic mosaicism, which in the brain may contribute to generating neuronal diversity in normal and disease conditions[1–3]. Moreover, recent studies have demonstrated that brain somatic mutations can cause neurodevelopmental and neuropsychiatric disorders, including the cortical malformation Focal Cortical Dysplasia (FCD)[4,5]. Focal Cortical Dysplasia type II (FCDII) commonly causes pediatric epilepsy resistant to antiseizure medication necessitating neurosurgical resection of the epileptogenic zone, and is the most prevalent cortical malformation in pediatric epilepsy surgery[6]. FCDII lesions can affect small distinct cortical areas or extend to entire hemispheres, as in hemimegalencephaly. FCDII is characterized by the focal disruption of cortical lamination and the presence of characteristic cytomegalic cells, namely dysmorphic neurons (DN) and balloon cells (BC), which are intermingled with cells with normal morphologies[7]. DN contribute to epileptic discharges, and present an enlarged soma with a cytoplasmic accumulation of neurofilaments and Nissl substance[8]. BC have large cell bodies with opalescent cytoplasm devoid of Nissl substance, and their role in seizure generation remains uncertain. Recently, deep sequencing of surgically resected brain tissue has revealed somatic mutations in mTOR pathway genes in up to 60% of FCDII cases[9]. FCDII-causing mutations are either somatic gain-of-function single hits in genes coding for pathway activators (*e.g.*, *MTOR*, *PIK3CA*, *AKT3*, *RHEB*), or loss-of-function double-hits (germline and somatic) in genes coding for inhibitors of this pathway (*e.g.*, *DEPDC5*, *TSC1/2*)[10–14,9]. The proportion of mutated cells within the tissue correlates with the size of the lesion[9]. These postzygotic mutations are thought to arise during corticogenesis in dorsal pallium progenitors lining the ventricular zone[15] and to give rise to cytomegalic cells due to mTOR hyperactivation, a pathway that regulates cell growth and metabolism[16]. We and others have shown that DN and BC carry identical mTOR-activating mutations, implying a common origin from a single mutation event during development[12,17]. Yet, the mechanisms by which DN and BC contribute to epilepsy, and whether they represent distinct cell types or instead different states of a single cell type is mostly unknown. Moreover, a remaining challenge is to address the extent to which seizures reflect abnormal function of cytomegalic cells or non-cell autonomous effects of mutated on neighboring neurons. While several bulk transcriptomic studies of FCDII tissues have been conducted[18–21], single-cell resolution is essential to resolve the etiopathogenesis of FCDII in which only a few cells is mutated due to somatic mosaicism.

To address these questions, we used single-nucleus genotyping and transcriptomic analyses on 10 FCDII surgical brain samples, and spatial transcriptomics for the further validation of identified biomarkers. Our results reveal that DN and BC are molecularly distinct from one another, with glutamatergic neuron-like and astrocyte-like identities, respectively. Remarkably, only a small fraction of mutated cells exhibits cytomegalic features, revealing low penetrance of FCDII-causing mutations. By comparing the molecular identity of different cell types in control and patient tissue, we identify the cell-type-specific transcriptional programs that are cell-autonomously and non-cell-autonomously triggered by the mutation, and we highlight a critical role in the dysregulation of mitochondrial metabolism pathways in cytomegalic neurons.

RESULTS

The overall goal of this study was to investigate cell-type-specific transcriptional dysregulations in FCDII tissues by combining several transcriptomic approaches, focusing on epilepsy-associated alterations and mTOR-driven changes, and identifying disease-related biomarkers (**Fig. 1a**). For this purpose, we collected fresh frozen surgical cortical samples from 10 children who underwent neurosurgery to treat drug-resistant focal epilepsy and three postmortem cortical samples from non-epileptic age-matched controls (**Supplementary Table 1**). All patients had either somatic gain-of-function variants in *MTOR* (n = 5) or *RHEB* (n = 2), or loss-of-function germline and somatic variants in the mTOR inhibitor *DEPDC5* (n = 3). Patients received a neuropathological diagnosis of FCDII, either FCDIIa with only dysmorphic neurons (DN; all *DEPDC5* cases and one *MTOR* case) or FCDIIb with both DN and balloon cells (BC; *MTOR,* and *RHEB* cases) (**Extended Data Fig. 1a**). The variant allele frequency (VAF, reflecting the percentage of mutated alleles) ranged from 3% in patients with focal lesions to 17% in patients with hemispheric lesions (**Fig. 1b**). DN and BC displayed mTOR hyperactivity as revealed by phosphorylated S6 (pS6) immunostaining, a readout of mTOR signaling activation (**Extended Data Fig. 1b**).

Cell-type-specific transcriptional changes in FCDII surgical tissues

We performed single-nucleus 3' RNA sequencing (snRNA-seq) of cortical tissues using the 10X Genomics technology, which yielded 178,057 quality-controlled single nuclei from the 10 patients and the three non-epileptic controls. To expand the control dataset, we also integrated eight age-matched neurotypical controls from a previous study[22], and analyzed the distribution of all 184,007 nuclei (43,355 control nuclei; 140,652 patient nuclei) according to their transcriptional profile using 2D-UMAP dimensionality reduction (**Fig. 1c**; **Supplementary Table 2**; **Extended Data Fig. 2;** see Methods for integration of the datasets). Based on the expression of known cell-type markers and k-nearest neighbors (KNN) cell-type predictions built on the control age-matched dataset, we identified seven major cell types: glutamatergic neurons and GABAergic interneurons (derived from medial (IN-MGE) and caudal (IN-CGE) ganglionic eminences), astrocytes, oligodendrocytes, oligodendrocyte precursor cells (OPC), microglia, and endothelial cells (**Fig. 1c**). The relative proportion of these cell types was different between FCDII patient and control tissues. Notably, microglial cells, oligodendrocytes, and OPCs were overrepresented in FCDII samples, possibly reflecting differences in the surgical sampling between controls (postmortem tissue in which the cortical area can be precisely dissected) and patients (postoperative tissue with broader margins of resection within the white matter) (**Fig. 1c**; **Extended Data Fig. 1c,2b**).

Our data show that cell types largely overlapped between patients and controls, as we did not observe additional cell clusters common to all patients, although a subset of glutamatergic neurons was enriched in two patients (**Fig. 1d**, **Extended Data Fig. 2c)**. To examine how molecular pathways are affected in a cell-type-specific manner, we investigated the differentially expressed genes (DEGs) in patients compared to non-epileptic controls for each cell type. We observed broad transcriptional changes, with glutamatergic neurons and astrocytes showing the highest number of DEGs (n = 91 DEGs in GluN, n = 96 DEGs in astrocytes), while GABAergic interneurons were the least affected (n =

25 DEGs in IN-CGE and n = 35 DEGs in IN-MGE) (**Fig. 1e, Supplementary Table 3**). Remarkably, most DEGs were unique to individual cell types and Gene Ontology (GO) enrichment analysis revealed distinct dysregulated pathways across cell types (**Fig. 1e, Extended Data Fig. 3**), indicating a strong cell-type-specific component to FCDII pathogenesis. For example, in the GluN cluster of FCDII patients, we observed downregulation of *GRIN1* and *PRRT2*, two genes causing monogenic forms of focal epilepsies, and upregulation of *GLUL*, pointing towards alterations of the glutamate signaling and neurotransmission in glutamatergic neurons. Enriched GO terms in the GluN cluster were mostly associated with neurodevelopment, neurotransmission, and synaptic function (*e.g., SYT4*, *NPTXR*, *NRXN2*, *STX1A*, **Fig. 1f**). Together, these results reveal disease-relevant, cell-type-specific molecular dysregulations in the epileptic tissue, likely reflecting and/or contributing to circuit dysfunction and seizure activity.

Distribution of FCDII pathogenic mutations across cell types

We next assessed which cell types carry FCDII-causing somatic mutations and how this affects gene expression. To determine genotypes at single-cell resolution, we used 3' snRNA-seq data and targeted PacBio long-read sequencing of barcoded snRNA-seq transcripts. Overall, we genotyped n = 808 nuclei with high confidence, largely obtained from patient pt10 (78%), presenting a large FCDII (**Supplementary Table 4**). Since the VAF reflects the proportion of mutated cells within the resected tissue, our data showing that approximately 15% of genotyped nuclei were mutation-positive aligns with the VAF of around 9% identified in this patient. Mutation-positive nuclei predominantly clustered with glutamatergic neurons (25% GluL2/3 and 22% GluN) (**Fig. 2a**). A fraction of mutated nuclei was also assigned to astrocytes (22%), GABAergic interneurons (16% CGE-derived and 6% MGE-derived), oligodendrocytes (13%), microglia (11%), and OPCs (10%). mTOR activation was confirmed by pS6 immunoreactivity not only in neurons, but also in a few astrocytes, oligodendrocytes, and microglial cells (**Fig. 2b**). Hence, while disease-causing mutations can be distributed across different cell types, they are enriched in the glutamatergic neuronal and astrocytic lineages.

The crucial role of the mTOR pathway in regulating cell growth raises the question of the extent to which mutated cells exhibit a cytomegalic phenotype in FCDII. We therefore examined what proportion of mutated cells displayed cytomegalic features. For each patient, we compared the fraction of DN/BC with that of mutated cells (estimated from the VAF of the somatic variant). DN and BC were identified by their expression of the canonical SMI311 and VIM markers, respectively, as well as by morphological criteria (soma longest diameter ≥ 20µm) (**Fig. 2c**). This approach revealed that less than 10% of mutated cells are DN or BC (**Fig. 2c,d**). Overall, DN and BC represent only about 0.5% of all cells within the resected FCDII tissues (**Supplementary Table 5**), likely explaining the absence of distinct cell clusters for DN and BC in the UMAP space (**Fig. 1d**) despite their striking abnormal morphological appearance. Hence, we discovered that most mTOR-mutated cells are not cytomegalic DN/BC, indicating a low penetrance of the cellular overgrowth phenotype.

Cell-type-specific transcriptional dysregulation in FCDII mutated cells

To identify the cell-autonomous impact of transcriptional changes triggered by mTOR-activating mutations, we compared mutated cells to nearest neighbor non-mutated cells from patients, limiting the

analysis to cell types with at least 10 mutated cells: glutamatergic neurons (GluN and GluL2/6 clusters), astrocytes, and oligodendrocytes. DEG analysis showed cell-type-specific transcriptional changes, with the highest number of DEGs in GluN neurons (n = 296 genes) and in oligodendrocytes (n = 255 genes) (**Fig. 3a, Supplementary Table 6**). Among DEGs, n = 14 transcripts were annotated as part of the mTOR pathway in the KEGG database (**Fig. 3b**). While no significant GO-term enrichment was observed for dysregulated genes in mutated oligodendrocytes/microglia cells, gene set enrichment analysis of the genes upregulated in mutated compared to non-mutated GluN nuclei revealed alterations of pathways related to mitochondrial function, organization, metabolism respiration (*SUCLA2, HIGD1A, TFRC, GRSF1, FKBP8, VDAC1, PID1*), and synaptic vesicle endo/exocytosis (*SYNJ1*, *SNCG*, *AP2M1*, *PACSIN1*, *ARFGEF1*, *SCRN1*, *SYNGR3*, *RAB11A* and *GRIN3A*) (**Fig. 3c**). Mitochondrial metabolism and transport genes were also dysregulated in mutated astrocytes (*ACTR10*, *SYBU*, *MAP1B*, *ATCAY*, *DMGDH, AGPAT5, PHYKPL*) (**Extended Data Fig. 4**).

Non-cell-autonomous mechanisms causing hyperexcitability of non-mutated neurons located close to mutated ones have also been described in an FCDII mouse model[23]. To explore this scenario in human FCDII samples, we compared non-mutated GluN nuclei from patients to GluN nuclei from controls. We identified upregulation of genes involved in synaptic transmission and regulation of neuron projection development (**Fig. 3d**, **Supplementary Table 7**); ~90% of these genes were also upregulated in mutated GluN compared to control nuclei (including the epilepsy genes *SNAP25, CDKL5* and *DNM1,* as well as *DNM3*, *SLC24A2, NLGN4Y, SH3GL2, SNAP91, MAG, NDRG4, PAK1, IL1RAPL1 and MT3*) (**Extended Data Fig. 4**). This finding suggests that pathways related to synapse and neuronal circuits are indeed affected not only in mutated cells but also in non-mutated cells in FCDII. Together, these observations indicate two processes at play in FCDII with mTOR-activating mutation: 1) cell-autonomous mechanisms in mutated cells leading to abnormal mitochondria-related functions, and 2) non-cell-autonomous processes related to synaptic and neuronal circuit pathways in both mutated and non-mutated GluN (**Fig. 3e**).

DN and BC have glutamatergic neuron- and astrocyte-like transcriptional identities, respectively, and dysregulated metabolic pathways

DN and BC can be identified by histopathological markers such as SMI311 and VIM[15], but their comprehensive molecular identity remains unexplored. We thus applied several parallel approaches to determine the transcriptional identity of DN and BC: laser capture microdissection coupled with transcriptome-wide profiling (LCM-seq), and spatial transcriptomics using Visium and MERSCOPE technologies, the former providing whole transcriptome coverage albeit with limited spatial resolution, the latter allowing for subcellular resolution although limited to a targeted panel of selected genes.

First, we performed full-length SmartSeq mRNA sequencing of laser-captured pools of 160 DN (n = 8), BC (n = 2), and normal-appearing neurons (NN, n = 4), identified based on morphology and soma size (**Fig. 4a, Extended Data Fig. 5a, Supplementary Table 8**; Methods). Principal component and hierarchical cluster analyses on the top 2000 variable genes indicated that BC (expressing high levels of *VIM*) are molecularly distinct from NN and DN (expressing high levels of *NEFM*) (**Fig. 4a, Extended Data Fig. 5b**). Using label transfer, we integrated these cell pools into the snRNA-seq UMAP

space to identify the nearest cell type identities. DN and NN were predicted as GluN nuclei, while BC clustered with astrocytes (**Fig. 4b**). Accordingly, immunofluorescence staining revealed that DN (identified as pS6- and SMI311-expressing cells) expressed the GluN-enriched protein NRGN, and BC (identified as pS6- and VIM-expressing cells) expressed the astrocytic marker GFAP (**Fig. 4c**).

To introduce spatial resolution to our analysis, we performed Visium spatial transcriptomics on frozen cortical sections from three patients. On average, we analyzed n = 2,992 spots per sample and n = 2,846 genes from 4-5 cells per spot. Across samples, we morphologically identified DN and BC in n = 475 and n = 159 spots, respectively, which expressed higher levels of the known DN (neurofilament encoding genes *NEFH/M/L)* and BC markers (*CRYAB*) (**Fig. 4d,e**, **Extended Data Fig. 6**). Semi-supervised clustering highlighted differences in the spatial distribution of spots containing DN and BC across tissues (**Fig. 4f, Extended Data Fig. 6b**). DN-containing spots were predominantly located amongst glutamatergic neurons in all cortical layers. In contrast, BC-containing spots were disseminated throughout the tissue (**Extended Data Fig. 6**). These findings further support the hypothesis that DN relate to glutamatergic neurons, while BC cells distribute across the white and grey matter, as astroglial cells do.

To identify novel biomarkers of DN and BC, we combined LCM-seq and Visium data with snRNA-seq analyses (see methods). This approach identified genes encoding mitochondria-associated proteins in both DN and BC (*e.g., COX7A and VDAC1* in DN, and *AGPAT5* in BC), genes associated with neurotransmitters transport (*e.g., SNAP25*, *SLC38A1,* and *SLC1A1*) and apoptosis (*e.g.*, *OLFM1*, *LGALS1* and *TFRC*) in DN and genes associated with regulation of vesicle organization and fusion (*e.g., TRAPPC6B*, *CAV1*, *ANXA1* and *ANXA2*) or regulation of cell migration (*e.g., SDCBP*, *HGF* and *TNC*) in BC (**Extended Data Fig. 7**). We next used a MERSCOPE spatial transcriptomics approach to achieve a better cellular resolution and confirm some of the novel DN and BC biomarkers identified above. We designed a panel of probes targeting 140 genes, including canonical markers for cell type annotation, previously reported histological markers for DN/BC, and novel DN/BC candidate markers identified in our snRNA-seq, LCM-seq and Visium datasets (**Supplementary Table 9**). We used frozen cortical samples from 2 patients and identified DN and BC based on pS6 and NeuN proteins immunofluorescence. Because of the transcriptional proximity of DN and BC to GluN and astrocytes, respectively, we compared gene expression between DN (cytomegalic pS6 and NeuN-positive), BC (cytomegalic pS6-positive, NeuN-negative), normal-sized GluN (pS6-negative, NeuN-positive, expressing *NRGN*), and astrocytes (pS6-negative, NeuN-negative, expressing *AQP4*). Using this approach, we observed that DN and BC clusters were distinct from GluN and astrocytes in the UMAP space, suggesting that the custom panel is suitable to differentiate cytomegalic DN/BC from other cells in FCDII tissues (**Fig. 4g**). Of the 41 known histological DN/BC markers, we validated 22 genes at the transcriptional level (*e.g.,* increased expression of *NEFH* and *SLC32A1* and decreased expression of *SLK* in DN; increased expression of *VIM*, *CRYAB* and *GPNMB* in BC) (**Extended Data Fig. 7a**). The top 10 genes driving the clustering of DN and BC included six of the previously reported histological markers (*NEFM/H/L*, *GPNMB*, *VIM*, *CRYAB*), as well as new candidates, such as *SLC1A1* and *STMN2* in DN (encoding a glutamate transporter and a microtubule stability regulator, respectively), or *MFAP4* and *IGFBP7* in BC (encoding an extracellular matrix protein enriched in progenitor cells, and an insulin-

like growth factor binding protein associated with cellular senescence, respectively) (**Fig. 4h, Extended Data Fig. 7b**). Since mitochondrial genes were enriched in mutated GluN (**Fig. 3c**), we assessed the expression of mitochondrial genes in the MERSCOPE panel and confirmed their expression in DN (*e.g.*, *HGF*, *PID1*, *TFRC* and *VDAC1*) (**Extended Data Fig. 7c**). Pathways associated with metabolism, mitochondrial function, cell respiration, and ribonucleotide metabolism were also enriched in the analysis of 57 genes upregulated in DN, which were identified through the intersection of LCM-seq and Visium datasets with DEGs between snRNA-seq mutated and non-mutated GluN nuclei (**Fig. 4i**, **Supplementary Table 10**). To evaluate if such transcriptional upregulation was associated with increased mitochondrial biomass in DN, we assessed VDAC1 levels by immunofluorescence in FCDII tissues and observed strong VDAC1 immunoreactivity in pS6-positive DN (**Fig. 4j**).

Ultrastructural examination of DN from two postsurgical FCDII tissues by electron microscopy revealed cytoplasmic accumulation of intermediate filaments (likely neurofilament) and structurally damaged mitochondria with a vesicular-swollen morphology (and only occasional morphologically-normal mitochondria), compared to normal pyramidal neurons, while mitochondria of normal morphology were observed in BC (**Fig. 4k, Extended Data Fig. 8a-c**). We also observed rare neurons with an intermediate phenotype: normal soma size and mitochondrial number and structure, but with an aberrant accumulation of intermediate filaments (**Extended Data Fig. 8d**).

Overall, these findings suggest an accumulation of damaged mitochondria in the cytoplasm of DN, which may reflect recycling impairment due to the presence of mTOR-hyperactivating variants.

DISCUSSION

In this study, using a comprehensive identity profiling at the genomic, transcriptomic and morphological levels, we uncover the origin of pathogenic cytomegalic cells in FCDII and the autonomous and non-cell autonomous effects of somatic mutations on these cells and the circuit as a whole. We show that dysmorphic neurons (DN) are molecularly closely related to glutamatergic neurons, while balloon cells (BC) are instead more closely related to astrocytes. Hence, rather than representing different states of a single cell type, DN and BC are distinct cell types that likely emerged from a single mutational event prior to the divergence of the neuronal and astroglial lineages.

DN exhibit characteristics of molecularly dysfunctional glutamatergic neurons: they express high levels of neurofilaments, lack specific cortical layer markers, display mitochondrial abnormalities and show synapse-associated transcriptional alterations that may account for their previously reported intrinsic excitability[24]. The nature of differentially expressed genes between DN and BC suggests that they contribute to epileptogenesis *via* different mechanisms: DN display molecular hallmarks of hyperexcitability (including the glutamate transporter *SLC1A1*) and may thus affect non-mutated circuit partners through synaptic transmission, while BC display stronger expression of genes coding for secreted proteins (such as *MFAP4* and *IGFBP7*) that may affect neighboring cells in a paracrine manner. Notably, IGFBP7, a component of the senescence-associated secretory phenotype (SASP), further supports a critical role for cellular senescence in FCDII[25]. Interestingly, while both DN and BC consistently show increased mTOR pathway activation (as indicated by pS6 protein levels), only few

transcripts of the pathway were dysregulated in these cells, suggesting that mTOR hyperactivation is not primarily transcriptionally driven.

Remarkably, our findings reveal that mTOR-activating mutations cause cytomegaly in only a minority of cells; penetrance for this particular trait is thus incomplete, and DN or BC only represent the visible "tip of the iceberg" of mutated cells in FCDII tissues (<10% cells). Other mutated cells, however, may display different attributes, such as misorientation and mislocalization, potentially accounting for dyslamination in FCDII, or display abnormal electrophysiological properties without overt morphological features. The molecular mechanisms accounting for such variability in the cellular effects of mTOR activation are unknown but could depend on the timing of the mutation (including in a dose-dependent manner) or on cell-type-specific factors. The cellular environment could also influence the cellular phenotype in a non-cell autonomous manner, as supported by a recent study showing that wild-type cells suppress aberrant growth induced by oncogenic Ras mutations[26].

In addition to glutamatergic neurons and astrocytes, a small subset of cells from other lineages are also mutated, including GABAergic neurons and microglia. Most GABAergic neurons in the cortex originate from the ganglionic eminences, although recent studies have suggested that a portion of interneurons may have a dorsal origin[27–30], while microglia derive from the mesoderm. This finding implies that FCDII lesions (at least the more extended ones, with high VAF) would originate from mutations that presumably occurred prior to the separation of these cell types into different lineages (*i.e.* at the time of gastrulation, at gestational weeks 2-3, when the neurectoderm arises)[31]. Consistent with these findings, a recent study also reported that a somatic *RHEB* mutation at high VAF was distributed across various brain cell types in a patient with FCDII, suggesting a pre-gastrulation mutational event[32]. Nonetheless, further investigations will be needed to elucidate if small FCDII with lower VAF mutations also occurred at such early developmental stages.

Although early-embryonic mutational events in principle affect multiple organs[33], FCDII somatic mutations are not typically found in patients' available tissues other than the brain (*e.g.,* the blood or saliva). To account for this discrepancy, it is possible that the mutation was initially widespread across cell lineages, but remained detectable only in the neural lineage due to the negative selection of mutated cells outside the central nervous system, as recently reported for cortical malformations associated with somatic gain of chromosome 1q[34].

Our study also identified cell-type-specific and widespread transcriptional alterations in non-mutated cells from patient tissues, with dysregulated pathways related to neurodevelopment, neurotransmission, and synapse in glutamatergic neurons. In mutated glutamatergic neurons, cell-autonomous transcriptional changes instead involved altered metabolism and mitochondrial function. Using ultrastructural microscopy of cytomegalic cells in FCDII cortical tissues, we confirmed substantial abnormalities in DN, including accumulation of structurally damaged mitochondria. DN and BC are also pathognomonic cells observed in a related disorder, tuberous sclerosis complex (TSC). This finding is thus consistent with a previous study reporting an accumulation of damaged mitochondria in neurons lacking *TSC1/2*, which are components of an mTOR pathway inhibitory complex whose functional loss is associated with TSC[35]. Likewise, a recent study reported increased oxidative stress mediated by

reactive oxygen species and neuroinflammation (suggesting mitochondrial dysfunction) in patients with FCDII or TSC[36]. Therefore, the accumulation of damaged mitochondria in DN could result from excessive mTOR activity on mitochondrial biogenesis and fission[37], as well as mTOR-mediated accumulation of free radicals through increased oxidative phosphorylation[38].

To conclude, our study provides novel insights into the cellular and molecular complexity of FCDII, implicating altered mitochondrial function in dysmorphic neurons. mTOR hyperactivation in FCDII tissues seems to accelerate processes related to cellular aging, such as mitochondrial energy production, senescence, and block of the autophagic clearance of damaged mitochondria[39]. Senescence- and mitochondria-targeted therapeutics may therefore represent a novel avenue in patients with FCDII, potentially offering an alternative to invasive resective neurosurgery in the future.

METHODS

Brain samples collection. Surgical samples were obtained from 10 children (aged from 3 months to 16 years) who underwent epilepsy surgery at the Rothschild Foundation Hospital (Paris, France) between 2016 and 2020. Seven patients underwent resection of the epileptogenic zone ("focal" patients) while three underwent hemispherotomy (functional disconnection of the two hemispheres with resection of frontal cortical tissue; "hemispheric" patients), necessitating the removal of part of the frontal lobe to access the connections between the two hemispheres. Both fresh (unfixed) snap-frozen and formalin-fixed paraffin-embedded (FFPE) tissues were obtained for each patient. Non-essential brain tissues, not required for neuropathological diagnostic, were designated for research use. All patients provided written consent on an approved Île-de-France II Committee of Protection of Persons protocol (ID-RCB/EUDRACT-2015-A00671-48). Brain samples were reviewed and classified by board-certified neuropathologists according to the International League Against Epilepsy (ILAE) classification of FCD[7,40]. Cryosections (20µm-thick) from the snap-frozen blocks were cut for neuropathology confirmation by hematoxylin and eosin (HE) staining in the tissue designated for molecular investigations. Genomic bulk DNA was extracted from blood samples and frozen brain sections according to standard procedures. Bulk RNA from snap-frozen tissues was extracted using the Maxwell RSC Tissue RNA kit (Promega). RNA integrity numbers (RIN) assessed on a Tapestation (Agilent Technologies) were between 6 and 8.3. Control material was obtained from three age-matched postmortem frontal lobe tissues of individuals without a history of seizures or other neurological disease (ct1-3). The mean age at death was 4.1 years (range 2 months to 10 years), with a mean postmortem interval of 7 hours before brain tissue collection (range 6.5h-7.5h). Brain tissue was frozen and stored at −80°C. The control tissues collection and usage adhered to the principles outlined in the Declaration of Helsinki and the Amsterdam UMC Research Code provided by the Medical Ethics Committee (authorization N° W21_295 # 21.326).

Genetic investigations. Genetic investigations on paired brain-blood samples have previously been reported for all patients except one[12,17,41]. For patient pt2, we performed hybrid capture sequencing of brain and blood DNA samples, targeting coding exons and exon-flanking junctions (10 bp), using a custom panel of 57 known/candidate FCD genes from Twist Bioscience. The libraries were sequenced on an Illumina NovaSeq 6000 sequencer (2x150bp) at the iGenSeq sequencing facility of ICM. Bioinformatic analysis and validation of the somatic variant were carried out as previously described[12].

Immunostainings. To quantify dysmorphic neurons (DN) and balloon cells (BC) (**Fig. 2d**), 20µm-thick cryosections were obtained from the frozen brain tissue utilized for genetic and RNA investigations. Immunohistochemistry was conducted using primary antibodies against VIM (Vimentin-V9, 1:200, Dako #M0725) and SMI311 (1:200, BioLegend #837801), and revealed using the POLYVIEW (AP) and HIGHDEF green (anti-mouse) kit (Enzo Life Sciences). Sections were counterstained with DAPI and scanned in both brightfield and fluorescence channels with a Nanozoomer scanner (Hamamatsu) at 40X. Images were exported at 10X and 20X magnifications with the NDP.view2 software. For immunohistochemistry on 4µm FFPE sections, a primary antibody against $pS6^{240/244}$ (1:2000, Cell Signaling #5364) was used, employing an avidin-biotin peroxidase complex conjugation system

(Vectastain ABC Elite; Vector laboratories) and DAB as chromogen. Sections were counterstained with hematoxylin and processed as described above. Co-immunofluorescence was performed using primary antibodies against $pS6^{240/244}$ (1:1000, Cell Signaling #5364), VIM (1:100, Dako M0725), SMI311 (1:500, BioLegend #837801), GFAP (1:200, Thermo Fisher MA5-15086), NRGN (1:50, Thermo Fisher PA5-19209), OLIG2 (1:100, R&D Systems AF2418), IBA1 (1:500, Abcam ab5076), NeuN (1:500, Millipore MAB377), and VDAC1 (1:500, Abcam ab16814). Secondary antibodies included donkey anti-mouse Alexa 555 (1:1000, Thermo Fisher A31570), donkey anti-rabbit Alexa 647 (1:1000, Thermo Fisher A31573), and donkey anti-rabbit Alexa 488 (1:1000, Thermo Fisher A21206). Slides were counterstained with DAPI.

Cell proportion counting in frozen sections. Whole slide scans (in ndpi format) were imported into QuPath (v.0.3.2). The "cell detection" function was executed to automatically count DAPI-positive nuclei. Manual counting was performed for cells positive for SMI311 and VIM. Cell proportions were subsequently calculated by dividing the total count of SMI311- or VIM-positive cells by the number of DAPI-positive nuclei per section in each patient.

10X Chromium on human nuclei (snRNA-seq). To match histopathology with snRNA-seq data, we isolated nuclei from 150µm-thick frozen sections adjacent to the 20µm-thick cryosection used for hematoxylin and eosin (HE) staining. Approximately 40-60mg of frozen cortical tissues were homogenized with a dounce homogenizer, followed by nucleus isolation via a sucrose gradient. Subsequently, snRNA-seq was conducted on a droplet-based 10X Chromium platform (targeting 10,000 nuclei per sample), following the guidelines outlined in the Next GEM Single Cell 3' Reagent Kit v3.1 User Guide. Libraries were sequenced on an Illumina Novaseq 6000 sequencing platform at either the iGenSeq sequencing facility of ICM or the Genomics Core laboratory (KU Leuven), targeting 50,000 reads per nucleus. Raw fastq files were demultiplexed, aligned, and quantified using Cell Ranger v3, with a modified version of the GRCh38 human reference genome that includes intronic regions. Quality control filters were applied to snRNA-seq nuclei, including identification of non-empty droplets (DropletUtils R package), presence of less than 5% of mitochondrial reads, expression between 500 and 12,000 genes, and a minimum of 1,000 unique molecule identifiers (UMIs) identified. Only nuclei meeting these criteria were considered for downstream analysis.

Laser capture microdissection sequencing (LCM-seq). Laser capture microdissection (LCM) was conducted in an RNase-free environment according to a published protocol[45]. Pools of 160 cells were cut for balloon cells (BC), dysmorphic neurons (DN), and normal-appearing neurons (NN) from HE-stained frozen sections based on their morphology, as previously detailed[12]. Briefly, DN and BC were identified as cytomegalic cells (largest soma diameter >20µm), with or without Nissl substance cytoplasmic aggregates, respectively. NN with oval shape, largest soma diameter between 10-20µm and no Nissl substance aggregates were cut from perilesional regions, distant from cytomegalic cells. For DN and BC selection, we selected n = 5 samples with the best histological quality of the frozen sections and at least n = 50 DN/BC per section. Brain specimens from patients pt2 and pt4 comprised two pathological cortical gyri; therefore, we cut two separate DN pools as duplicate samples from distinct cortical regions (**Extended Data Fig. 5a**). Microdissected cells were collected in AdhesiveCap

500 Opaque tubes (Zeiss) within two hours from tissue staining, and RNA was extracted immediately with the RNA Tissue XS kit (Macherey-Nagel), following the protocol for LCM isolated cells, and eluting in 5µL of nuclease-free water. RNA samples were stored at -80°C until further processing. SmartSeq libraries were generated using the Nextera XT DNA Library Preparation Kit (low input) and run on a MiSeq Standard v2 cartridge (2x150bp). Transcript expression quantification was performed using Salmon (aligned on the human reference Genecode v36) and VST (variance stabilizing transformation) normalization. Mutated reads were manually inspected using Integrative Genome Viewer (IGV) at each mutation site to assess for the presence of the somatic mutation identified in each patient.

Dataset integration and cell type assignment. To ascertain the cell type identity of the sequenced nuclei (snRNA-seq) and of the Laser Capture Microdissection (LCM) sequencing samples, we utilized control cells from a previously published prefrontal cortex dataset as a reference (here referred to as V19)[22]. Specifically, we randomly selected n = 350 V19 control nuclei per cell type from individuals aged between 4 and 19 years old, aligning with the age range of our cohort (5538_PFC_Nova, 5387_BA9, 5408_PFC_Nova, 5936_PFC_Nova, 5893_PFC, 5879_PFC_Nova, 5976_BA9, 4341_BA46). To mitigate batch effects between V19 individuals, we executed Seurat v2 single-cell integration pipeline. Next, we integrated each in-house dataset onto V19 using a common set of 2000 variable genes across datasets. snRNA-seq and LCM samples were sequentially integrated with the V19 reference to optimize parameter tuning based on sample sizes. Finally, a common scaled data space was assembled across integrations (intra-V19, snRNA-seq-V19, LCM-V19) and upon UMAP 2D embedding, we trained a cross-validated (10 folds) 200-nearest neighbors' classifier on V19 cell coordinates, achieving an 87% accuracy to predict the maximum likelihood cell type of in-house integrated samples. Cell type annotation was slightly adjusted based on a recent publication[42]: “NRGN-I”, “NRGN-II” and “Mat.Neu.” V19 annotations were here categorized under “GluN”, while “Ast-PP” and “Ast-FB” were combined and labeled as “Astrocytes”.

UMAP plots and cell type proportions. To illustrate the distribution of nuclei based on age and to depict single individual UMAPs, 500 random nuclei per control/patient from our dataset were plotted alongside with 500 random nuclei from the control reference dataset (V19; by age: 4y n = 29; 6y n = 53; 12y n = 147; 13y n = 78; 14y n = 46; 15y n = 38; 19y n = 109). To display the distribution of nuclei according to dysplasia type (*i.e.*, control, focal or hemispheric dysplasia), disease group (*i.e.*, patients *vs.* controls), or predicted cell types, the same number of nuclei per individual was randomly selected, resulting in a total of 3000 nuclei per phenotype (*i.e.*, n = 4 controls: n = 750 nuclei/individual; n = 3 hemispheric: n = 1000 nuclei/individual; n = 7 focal: n = 430 nuclei/individual; n = 10 patients: n = 300 nuclei/individual). LCM samples (n = 8 DN, n = 4 NN and n = 2 BC) were plotted alongside control (n=3000) nuclei (n = 750 from each in-house control individual and n = 750 from the V19 dataset).

snRNA-seq nuclei genotyping. To identify mutation-carrying nuclei in snRNA-seq data from all samples, we manually inspected the somatic mutation sites in each patient using IGV and extracted the barcode ID of mutated nuclei. We used cb_sniffer to list the nuclei barcodes for which the mutation site was covered and retrieve nuclei with reference-only alleles. To overcome the limited coverage of the mutation sites in the single-cell 3' sequencing experiment, we adapted a previously reported

approach[44], integrating high-throughput single-cell gene expression analysis from the 10X Genomics snRNA-seq platform with targeted PacBio long-read sequencing of barcoded transcripts. We performed long-read targeted sequencing and analysis of 10X cDNA from patients pt6, pt8 and pt10 at the Gentyane facility (France). 50ng of single-nuclei cDNA from 10X Genomics was subjected to 4-6 PCR cycles using NEBNext Ultra II Q5 Master Mix (New England Biolabs, #M0544L) with recommended NEB NGS PCR thermocycling conditions, and PCR products were purified with 0.9X SPRIselect paramagnetic beads. A custom probe gene panel (*PIK3CA, PTEN, AKT3, MTOR, TSC1, TSC2, DEPDC5, NPRL3, RHEB, SLC35A2, BRAF, NPRL2*) (Twist Biosciences) was used for capture hybridization, with 850 ng of cDNA for 16 hours. Post-capture 16-cycles PCR was performed using NEBNext Ultra II Q5 Master Mix (New England Biolabs, #M0544L) at 69°C annealing temperature. PCR products were then purified using the SPRIselect 1X and used for SMRTbell library preparation with the SMRTbell Express Template Prep Kit 2.0 according to PacBio Amplicon protocol. Circular consensus sequencing (CCS) reads were generated from raw data using ccs (~99.9% precision), and long-read samples were demultiplexed using lima (version 2.7.1). Sequences were analyzed using a custom pipeline to recover the barcodes of mutated and non-mutated nuclei: 1) reads were aligned with minimap2 (version 2.24) against the hg38 human genome reference to obtain BAM files; 2) patient-specific variant alleles were retrieved for each read using the GenomicAlignements R module; 3) reads were demultiplexed for 10X barcodes from each patient using the script seal.sh from the BBtools v38.96 suite (only barcodes with 100% identity were recovered). Each mutation site was manually verified on IGV to check for high quality and high confidence in variant calling.

Differential gene expression analyses. 1) *Patients vs. controls.* The analysis was restricted to patients with focal lesions for the following reasons: (i) older age at surgery, suggesting a more mature neuronal network, and (ii) resected tissue located at the center of the epileptogenic focus compared to less specific location of tissue resected after hemispherotomy in patients with hemispheric lesions. For each cell type, we compared gene expression in nuclei from focal patient to age-matched control nuclei (aged 2 to 19 years old), using the same number of randomly selected nuclei per individual and per phenotype: Astrocytes: n = 350 nuclei/individual; Oligodendrocytes: n = 200 nuclei/control, n = 65 nuclei/patient; Microglia: n = 200 nuclei/control, n = 300 nuclei/patient; GluN: n = 350 nuclei/control, n = 80 nuclei/patient; IN-CGE: n = 350 nuclei/individual; IN-MGE: n = 350 nuclei/individual; GluL2/3: n = 350 nuclei/control, n = 150 nuclei/patient; GluL4: 350 nuclei/control, 200 nuclei/patient; GluL5/6: n = 350 nuclei/control, n = 250 nuclei/patient. Gene ontology analysis was conducted per cell type using the gseGO function of the clusterProfiler R package[43] on genes expressed in more than 25% of cells with more than 0.4 absolute log2 Fold Change (log2FC) expression. To enhance readability, gene ontologies were labeled by family (*e.g.* “modulation of chemical synaptic transmission”, “regulation of synaptic plasticity” and “regulation of trans-synaptic signaling” are labeled as “regulation of synaptic plasticity”). 2) *Mutated vs non-mutated.* We compared gene expression for GluN, GluL2-6 (GluL2/3, GluL4 and GluL5/6), astrocytes and oligodendrocytes mutated and non-mutated nuclei from patients pt9 and pt10 (with *RHEB* mutation). GluN: n = 29 mutated (pt9: 8; pt10: 21) and n = 92 non-mutated nuclei (pt9: 7; pt10: 85); GluL2-6: n = 22 mutated (pt9: 12; pt10: 10) and n = 127 non-mutated nuclei (pt9: 9; pt10: 118); Astrocytes: n = 17 mutated (pt9: 1; pt10: 16) and n = 50 non-mutated nuclei (pt10

only); Oligodendrocytes (pt10 only): n = 17 mutated and n = 101 non-mutated nuclei. Gene ontology analysis was performed per cell type on genes expressed in more than 25% of cells with more than 0.3 absolute log2FC expression, as described above.

10X Visium spatial transcriptomics. Standard Visium protocol (spot diameter = 55µm) and HE staining were performed on 10µm-thick frozen brain sections from patients pt2, pt5 and pt9. Libraries were sequenced on a NovaSeq 6000 SP cartridge (2X50bp), and raw data were analyzed with Space Ranger v2.0.0, aligned with the reference genome "refdata-gex-GRCh38-2020-A". Following a standard analysis run, each output was manually inspected on the Loupe Browser to manually select tissue-overlapping spots, and spots containing DN or BC were annotated. Data were then analyzed using Seurat v4.1.1. Spots with <200 detected genes, <500 reads, >40% mitochondrial genes, >20% hemoglobin genes and >5% ribosomal genes were filtered out, and mitochondrial genes (MT-) were removed. Data were normalized with Seurat's SCTransform. PCA reduction was performed using the marker genes (**Supplementary Table 5**) from a previously published control Visium dataset[46]. UMAP reduction and clustering were conducted with standard Seurat functions, with a resolution of 0.4, 0.2 and 0.4 for patients pt2, pt5 and pt9, respectively. Spatial clusters were annotated based on the predominant cell type contributing to the top expressed genes in the cluster (identified using the FindAllMarkers function in Seurat). When more than one cluster was predominantly characterized by the same cell type, the top expressed marker was included in the annotation for their distinction. Cell type prediction and deconvolution were performed with CytoSPACE v.1.0.1[47] to estimate the number of cells per spot. The “AddModuleScore” Seurat function was used to evaluate the expression pattern of cortical layer markers per spot, based on the gene lists provided by a previously published control Visium dataset[46].

Identification of DN and BC dysregulated genes using LCM-seq and Visium spatial transcriptomics. Expression of dysregulated genes identified with snRNA-seq in GluN and astrocytes mutated nuclei was analyzed in LCM-seq samples and Visium spots corresponding to DN and BC. Genes that were down- or up-regulated in GluN mutated nuclei, LCM-seq DN pools and Visium DN spots were categorized as DN down- or up-regulated genes, respectively. Genes that were down- or up-regulated in astrocytes mutated nuclei, LCM-seq BC pools and Visium BC spots were categorized as BC down- or up-regulated genes. Gene ontology analysis was performed on DN and BC up-regulated genes as described above.

MERSCOPE panel design, tissue preparation and analysis. We designed a custom panel of 140 genes, comprising 67 novel putative biomarkers of DN (n = 30) and BC (n = 37) selected across snRNA-seq, LCM-seq and Visium data (**Supplementary Table 9**). For DN, we compared DN *vs.* NN from the LCM-seq, and GluN mutated *vs.* non-mutated from the snRNA-seq and selected upregulated genes that were common across samples and enriched in Visium spots containing DN. For BC, we identified top expressed genes shared by the two LCM-seq BC samples, upregulated genes in the astrocytes mutated *vs.* non-mutated snRNA-seq and confirmed in Visium spots containing BC. The panel also included 16 cell type markers, 7 mTOR pathway genes, 9 senescence-associated genes[48] and 41 DN/BC putative markers from the literature. Frozen brain samples from patients pt5 and pt9 were

selected for the experiment and processed according to standard protocol: 10µm-thick tissue sections were cryostat-cut at -18°C, affixed to MERSCOPE slides for MERFISH with 250nm optical resolution, fixed, and dispatched to Vizgen (Cambridge, USA). Sections were stained with DAPI to mark nuclei, and antibodies against NeuN and $pS6^{240/244}$ to distinguish DN (NeuN/pS6 double-positive cells) and BC (pS6-positive, NeuN-negative cells). Regions of interest (ROIs), manually delineated on the MERSCOPE visualizer around single DN (n = 100, 50 from each patient), BC (n = 100, 50 from each patient), astrocytes (n = 50 from pt5) and GluN (n = 100, 50 from each patient), were based on NeuN/pS6 immunoreactivity and expression of known markers (*NEFM* for DN, *VIM* for BC, *AQP4* for astrocytes and *NRGN* for GluN). Gene expression matrix and coordinates were exported for each ROI and assembled in a Seurat object for gene expression analysis. Briefly, we exported the raw gene counts per ROI for the 140 genes and processed single-cell expression following the Seurat v4 pipeline: 1) SCTransform gene count normalization to the total expression; 2) highly variable genes detection and principal component analysis; 3) graph-based clustering (with the 10 first principal components and a clustering resolution of 0.5); 4) UMAP calculation. Heatmaps of SCT normalized gene expression data for known and novel markers were generated using the ComplexHeatmap package in R.

Electron microscopy. Following surgical removal, $5mm^3$ of postoperative brain tissue from patients pt4 and pt5 was immediately fixed in a solution of 2% glutaraldehyde, 2% paraformaldehyde, and 2mM CaCl2 in 0.1M sodium cacodylate buffer at pH 7.4 for 1hr at room temperature (RT). Tissues were post-fixed for 1hr at RT in 1% osmium tetroxide (aqueous solution) and contrasted with 2% aqueous uranyl acetate. Pieces of grey matter were dissected, progressively dehydrated in ethanol solutions and acetone, and embedded in Epon resin. Polymerization was carried out for 48h at 56°C in a dry oven. Semi-thin sections (0.5µm-thick) were cut and stained with 1% toluidine blue in 1% borax, and ultra-thin sections (70nm-thick) were contrasted with Reynold's lead citrate. Imaging was performed with a Hitachi HT7700 electron microscope at 70 kV and images were captured with an AMT41B camera.

ACKNOWLEDGEMENTS

We thank the ICM core facilities ICM.Quant, Histomics, iGenSeq, DAC and the DNA and cell bank; and the Gentyane sequencing facility (Vincent Pailler). We thank Eric Noé, Agnès Rastetter, Lilly Kaufmann and Dominique Langui for technical assistance. We thank the clinical research service of the Rothschild Foundation Hospital for assistance in the recruitment of patients. We thank the patients and their families.

AUTHOR CONTRIBUTIONS

S.Bal., E.K., L.G.T, M.D., C.R., S.R.P., S.Biz., L.S. and T.R. participated in experimental investigations and analyses. M.C., H.A.B., and E.A. recruited patients and provided human biological resources. S.Bal. and S.Bau. designed the study, drafted and revised the manuscript. S.Bau. and D.J supervised the study. S.Bau obtained funding. All authors reviewed the manuscript before submission.

FUNDING

The project was supported by Rothschild Foundation Hospital, the European Union's Horizon 2020 research and innovation program under grant agreement No 824110 (EASI-Genomics PID:7712 to

S.Bau.), the French National Research Agency (ANR EPIDEV to S.Bau.), the program "Investissements d'avenir" (ANR-10-IAIHU-06 to S.Bau.), the Netherlands Organisation for Health Research and Development (ZonMw; project 09120012010007 to E.A.), the Swiss National Science Foundation (to D.J.), the Carigest Foundation (to D.J.), the Société Académique de Genève FOREMANE Fund (to D.J.), the European Research Council (to D.J.) and the NeuroNA foundation (to D.J.).

FIGURE LEGENDS

Fig. 1 | Cell-type-specific dysregulation of synapse and neurodevelopment pathways in FCDII.
a, Workflow of the study. Single-nucleus RNA sequencing (snRNA-seq) was employed to examine transcriptional changes related to epilepsy in FCDII tissues. Genotypes of mutation sites were examined within patients' nuclei to compare mutated and non-mutated cell lineages. Integration of these findings with spatial transcriptomics of FCDII tissues allowed for the correlation of transcriptional alterations with cellular dysmorphology and spatial disorganization. **b**, The subject cohort includes frozen brain tissues from ten patients (pt1-10) and three postmortem age-matched neurotypical controls (ct1-3). Dysplastic areas in pt1, 4, and 9 extended to an entire hemisphere, with pt4 and 9 diagnosed with hemimegalencephaly. “VAF” refers to the variant allele frequency of somatic mutations for each patient; na: not available (no somatic hit identified); yrs: years. Plus or minus signs indicate the presence or absence of dysmorphic neurons and balloon cells. Abbreviations: N., neurons; C., cells. **c**, Left: UMAP dimensionality reduction of integrated snRNA-seq data of patients and controls using previously published age-matched control nuclei [22]. Cell-type annotations were adapted from a prior study [22] (see methods). Dashed lines outline cluster densities. Right: Cell type proportions in controls and patients with focal or hemispheric dysplasia. Abbreviations: Glu, glutamatergic; N, neurons; L, layer; CC, cortico-cortical projection neurons; IN-MGE, interneurons originating from the medial ganglionic eminence; IN-CGE, interneurons originating from the caudal ganglionic eminence; OPC, oligodendrocyte precursor cells. **d**, UMAP visualization showing control and patient nuclei. Outlines of cluster densities are represented with dash lines. **e**, Cell-type-specific differential gene expression (DEG) analysis between patients with focal FCDII and controls. Left: Number of DEGs per cell type (DEGs; significant genes expressed in at least 25% of cells with absolute log2 fold change > 0.4). Middle: Specific and shared DEGs across cell types; examples of DEGs specific to one cell type are indicated. Right: Proportion of DEGs specific to one or more cell types. **f**, Top gene ontologies (GO) and associated genes for GluN differentially expressed genes.

Fig. 2 | Mutated cells are predominantly glutamatergic neurons and exhibit only occasional cytomegalic phenotypes.
a, Mutation-positive nuclei are distributed across various cell types in the UMAP space with an enrichment observed in glutamatergic neurons and astrocytes. Right: percentage of mutated nuclei per cell type (top) and percentage of mutated nuclei across cell types (bottom). Abbreviations: GluN, glutamatergic neurons; GluL2/3, glutamatergic neurons of layers 2 and 3; GluL4/6, glutamatergic neurons of layers 4 to 6; IN-MGE, interneurons originating from the medial ganglionic eminence; IN-CGE, interneurons originating from the caudal ganglionic eminence; Astro, astrocytes; Oligo,

oligodendrocytes; OPC, oligodendrocyte precursor cells; Micro, microglia; Endo, endothelial cells. **b**, Representative images of co-immunofluorescence staining on FFPE sections using pS6 to label mTOR-hyperactive neurons (NeuN+, pt2), astrocytes (GFAP+, pt2), oligodendrocytes (OLIG2+, pt2) and microglia (IBA1+, pt10). Nuclei (in blue) are labeled with DAPI. Scale bars = 20µm. **c**, A minor fraction of FCDII mutated cells exhibit cytomegalic features. Left: representative immunostaining of SMI311+ dysmorphic neuron (DN) and VIM+ balloon cell (BC) on frozen brain tissue from pt5, nuclei (in blue) are labeled with DAPI for total cell counting. Scale bar = 25µm. Right: percentage of mutated cells (inferred by the detected VAF) and proportion of DN/BC identified in each patient. Abbreviations: Hemi, hemispheric. **d**, Representative schematic of the distribution of mutated cells across cell types and the fraction of mutated cytomegalic cells in pt10.

Fig. 3 | Cell-type-specific transcriptional dysregulation in FCDII mutated cells.

a, Cell-type-specific differential gene expression analysis between mutated and non-mutated nuclei from patients. Top Left: Number of differentially expressed genes (DEGs) per cell type (significant genes expressed in 25% of cells with absolute logarithmic fold change (logFC) > 0.3). Top right: Specific and shared DEGs across cell types; examples of DEGs specific to one cell type are indicated. Bottom: Proportion of DEGs specific to one or more cell types. **b**, Absolute average logarithmic fold change (logFC) values for DEGs belonging to the mTOR signaling pathway from the KEGG database across cell types. **c-d**, Top gene ontologies (based on adjusted (adj.) p-values) with corresponding genes for up-regulated DEGs in mutated *vs*. non-mutated GluN (**c**) and in non-mutated *vs*. control GluN (**d**). Similar ontologies were grouped into one single term. **e**, Schematic of cell-autonomous metabolic alterations and non-cell-autonomous synaptic activity changes in FCDII.

Fig. 4 | Dysmorphic neurons and balloon cells belong to glutamatergic and astroglial lineages and display metabolic dysregulations.

a, Left: LCM-seq workflow for dissecting and sequencing pools of DN, BC and NN from 8 patients. Right: heatmap of VST normalized average gene expression of DN and BC marker genes NEFM and VIM, and unsupervised hierarchical clustering of LCM-seq samples. **b,** Label transfer of LCM-seq samples in the snRNA-seq UMAP space. NN and DN match with GluN, and BC with astrocytes. **c,** Left: heatmap of VST normalized average gene expression of NRGN and GFAP, markers of GluN and astrocytes, respectively. Right: Co-immunofluorescence staining showing NRGN protein in pS6-SMI311 double-positive DN, and GFAP in pS6-VIM double-positive BC in pt5. GFAP-pS6 and VIM-pS6 double-stainings were performed on two consecutive sections and the same BC was recognized in both sections. Nuclei (in blue) are labeled with DAPI. Scale bar = 50µm. **d,** Visium spatial transcriptomics: spots containing DN and BC are intermingled across the tissue in pt5. Magnified images of representative DN- and BC-containing spots after HE staining are provided. **e,** Top markers of DN- and BC-containing spots in pt5. Known histological markers for DN (NEFM) and BC (CRYAB) are enriched in spots with DN and BC. **f,** Spatial semi-supervised clustering of Visium spots from pt5 shows clusters enriched in glutamatergic neurons, astrocytes and oligodendrocytes. Genes in parentheses indicate the top markers of the clusters. **g,** MERSCOPE analysis of manually selected single cells from pt5 and pt9. Separate clusters for DN, BC, astrocytes (Astro) and GluN are identified in the UMAP space. **h,**

Heatmap of the SCTransform normalized average expression of the top 10 marker genes of DN and BC across pt5 and pt9 MERSCOPE data. Representative MERSCOPE images of these markers in DN and BC from pt5 are shown. DN are identified as pS6-NeuN double-positive; BC as pS6-positive and NeuN-negative. Scale bar = 50µm. **i,** Left: Number of GluN genes (dysregulated in mutated vs. non-mutated GluN nuclei from snRNA-seq) validated in DN by LCM-seq and Visium. Right: Top gene ontologies of DN up-regulated genes. **j,** Representative images of co-immunofluorescence staining of VDAC1 and pS6 proteins in pt2. Strong VDAC1 signal is detected in DN. Scale bar = 50µm. **k,** Electron microscopy of DN from pt5 shows accumulation of vesicular-swollen damaged mitochondria (black circles). Scale bar = 2.5µm.

REFERENCES

1. Evrony, G. D. One brain, many genomes. *Science* **354**, 557–558 (2016).
2. Bae, T. *et al.* Different mutational rates and mechanisms in human cells at pregastrulation and neurogenesis. *Science* **359**, 550–555 (2018).
3. Rockweiler, N. B. *et al.* The origins and functional effects of postzygotic mutations throughout the human life span. *Science* **380**, eabn7113 (2023).
4. Lee, J. H. Somatic mutations in disorders with disrupted brain connectivity. *Exp Mol Med* **48**, e239–e239 (2016).
5. Blumcke, I. *et al.* Neocortical development and epilepsy: insights from focal cortical dysplasia and brain tumours. *The Lancet Neurology* **20**, 943–955 (2021).
6. Blumcke, I. *et al.* Histopathological Findings in Brain Tissue Obtained during Epilepsy Surgery. *New England Journal of Medicine* **377**, 1648–1656 (2017).
7. Blumcke, I. *et al.* The clinico-pathological spectrum of Focal Cortical Dysplasias: a consensus classification proposed by an ad hoc Task Force of the ILAE Diagnostic Methods Commission. *Epilepsia* **52**, 158–174 (2011).
8. Macdonald-Laurs, E. *et al.* Intrinsic and secondary epileptogenicity in focal cortical dysplasia type II. *Epilepsia* **n**/**a**, (2022).
9. Gerasimenko, A., Baldassari, S. & Baulac, S. mTOR pathway: Insights into an established pathway for brain mosaicism in epilepsy. *Neurobiology of Disease* **182**, 106144 (2023).
10. Mirzaa, G. M. *et al.* Association of MTOR Mutations With Developmental Brain Disorders, Including Megalencephaly, Focal Cortical Dysplasia, and Pigmentary Mosaicism. *JAMA Neurol* **73**, 836–845 (2016).
11. D'Gama, A. M. *et al.* Somatic Mutations Activating the mTOR Pathway in Dorsal Telencephalic Progenitors Cause a Continuum of Cortical Dysplasias. *Cell Reports* **21**, 3754–3766 (2017).
12. Baldassari, S. *et al.* Dissecting the genetic basis of focal cortical dysplasia: a large cohort study. *Acta Neuropathol* **138**, 885–900 (2019).
13. Sim, N. S. *et al.* Precise detection of low-level somatic mutation in resected epilepsy brain tissue. *Acta Neuropathol* **138**, 901–912 (2019).
14. Chung, C. *et al.* Comprehensive multi-omic profiling of somatic mutations in malformations of cortical development. *Nat Genet* **55**, 209–220 (2023).
15. Lamparello, P. *et al.* Developmental lineage of cell types in cortical dysplasia with balloon cells. *Brain* **130**, 2267–2276 (2007).
16. Panwar, V. *et al.* Multifaceted role of mTOR (mammalian target of rapamycin) signaling pathway in human health and disease. *Sig Transduct Target Ther* **8**, 1–25 (2023).
17. Lee, W. S. *et al.* Gradient of brain mosaic RHEB variants causes a continuum of cortical dysplasia. *Annals of Clinical and Translational Neurology* **8**, 485–490 (2021).
18. Assis-Mendonça, G. R. *et al.* Transcriptome analyses of the cortex and white matter of focal cortical dysplasia type II: Insights into pathophysiology and tissue characterization. *Front Neurol* **14**, 1023950 (2023).

19. Bedrosian, T. A. *et al.* Detection of brain somatic variation in epilepsy-associated developmental lesions. *Epilepsia* **63**, 1981–1997 (2022).
20. Li, Y.-F. *et al.* Identifying cellular signalling molecules in developmental disorders of the brain: Evidence from focal cortical dysplasia and tuberous sclerosis. *Neuropathology and Applied Neurobiology* **47**, 781–795 (2021).
21. Zimmer, T. S. *et al.* Balloon cells promote immune system activation in focal cortical dysplasia type 2b. *Neuropathology and Applied Neurobiology* **47**, 826–839 (2021).
22. Velmeshev, D. *et al.* Single-cell genomics identifies cell type–specific molecular changes in autism. *Science* **364**, 685–689 (2019).
23. Koh, H. Y. *et al.* Non–Cell Autonomous Epileptogenesis in Focal Cortical Dysplasia. *Annals of Neurology* **90**, 285–299 (2021).
24. Cepeda, C., André, V. M., Vinters, H. V., Levine, M. S. & Mathern, G. W. Are Cytomegalic Neurons and Balloon Cells Generators of Epileptic Activity in Pediatric Cortical Dysplasia? *Epilepsia* **46**, 82–88 (2005).
25. Thom, M. *et al.* An Investigation of the Expression of G1-Phase Cell Cycle Proteins in Focal Cortical Dysplasia Type IIB. *Journal of Neuropathology & Experimental Neurology* **66**, 1045–1055 (2007).
26. Gallini, S. *et al.* Injury prevents Ras mutant cell expansion in mosaic skin. *Nature* **619**, 167–175 (2023).
27. Andrews, M. G. *et al.* LIF signaling regulates outer radial glial to interneuron fate during human cortical development. *Cell Stem Cell* **30**, 1382-1391.e5 (2023).
28. Chung, C. *et al.* Cell-type-resolved somatic mosaicism reveals clonal dynamics of the human forebrain. 2023.10.24.563814 Preprint at https://doi.org/10.1101/2023.10.24.563814 (2023).
29. Delgado, R. N. *et al.* Individual human cortical progenitors can produce excitatory and inhibitory neurons. *Nature* **601**, 397–403 (2022).
30. Kim, S. N. *et al.* Cell lineage analysis with somatic mutations reveals late divergence of neuronal cell types and cortical areas in human cerebral cortex. 2023.11.06.565899 Preprint at https://doi.org/10.1101/2023.11.06.565899 (2023).
31. Ghimire, S., Mantziou, V., Moris, N. & Martinez Arias, A. Human gastrulation: The embryo and its models. *Developmental Biology* **474**, 100–108 (2021).
32. Townsend, S. E. *et al.* Single-nuclei transcriptomics enable detection of somatic variants in patient brain tissue. *Sci Rep* **13**, 527 (2023).
33. Muyas, F. *et al.* De novo detection of somatic mutations in high-throughput single-cell profiling data sets. *Nat Biotechnol* 1–10 (2023) doi:10.1038/s41587-023-01863-z.
34. Miller, K. E. *et al.* Post-zygotic rescue of meiotic errors causes brain mosaicism and focal epilepsy. *Nat Genet* 1–9 (2023) doi:10.1038/s41588-023-01547-z.
35. Ebrahimi-Fakhari, D. *et al.* Impaired Mitochondrial Dynamics and Mitophagy in Neuronal Models of Tuberous Sclerosis Complex. *Cell Reports* **17**, 1053–1070 (2016).
36. Arena, A. *et al.* Oxidative stress and inflammation in a spectrum of epileptogenic cortical malformations: molecular insights into their interdependence. *Brain Pathology* **29**, 351–365 (2019).

37. Morita, M. *et al.* mTOR Controls Mitochondrial Dynamics and Cell Survival via MTFP1. *Molecular Cell* **67**, 922-935.e5 (2017).
38. de la Cruz López, K. G., Toledo Guzmán, M. E., Sánchez, E. O. & García Carrancá, A. mTORC1 as a Regulator of Mitochondrial Functions and a Therapeutic Target in Cancer. *Frontiers in Oncology* **9**, (2019).
39. Liu, G. Y. & Sabatini, D. M. mTOR at the nexus of nutrition, growth, ageing and disease. *Nat Rev Mol Cell Biol* **21**, 183–203 (2020).
40. Najm, I. *et al.* The ILAE consensus classification of focal cortical dysplasia: An update proposed by an ad hoc task force of the ILAE diagnostic methods commission. *Epilepsia* **63**, 1899–1919 (2022).
41. Baldassari, S. *et al.* The landscape of epilepsy-related GATOR1 variants. *Genet Med* **21**, 398–408 (2019).
42. Caglayan, E., Liu, Y. & Konopka, G. Neuronal ambient RNA contamination causes misinterpreted and masked cell types in brain single-nuclei datasets. *Neuron* **110**, 4043-4056.e5 (2022).
43. Wu, T. *et al.* clusterProfiler 4.0: A universal enrichment tool for interpreting omics data. *The Innovation* **2**, 100141 (2021).
44. Koboldt, D. C. *et al.* PTEN somatic mutations contribute to spectrum of cerebral overgrowth. *Brain* **144**, 2971–2978 (2021).
45. Nichterwitz, S., Benitez, J. A., Hoogstraaten, R., Deng, Q. & Hedlund, E. LCM-Seq: A Method for Spatial Transcriptomic Profiling Using Laser Capture Microdissection Coupled with PolyA-Based RNA Sequencing. in *RNA Detection: Methods and Protocols* (ed. Gaspar, I.) 95–110 (Springer, New York, NY, 2018). doi:10.1007/978-1-4939-7213-5_6.
46. Maynard, K. R. *et al.* Transcriptome-scale spatial gene expression in the human dorsolateral prefrontal cortex. *Nat Neurosci* **24**, 425–436 (2021).
47. Vahid, M. R. *et al.* High-resolution alignment of single-cell and spatial transcriptomes with CytoSPACE. *Nat Biotechnol* 1–6 (2023) doi:10.1038/s41587-023-01697-9.
48. Tuttle, C. S. L., Luesken, S. W. M., Waaijer, M. E. C. & Maier, A. B. Senescence in tissue samples of humans with age-related diseases: A systematic review. *Ageing Research Reviews* **68**, 101334 (2021).

Fig. 1 | Cell-type-specific dysregulation of synapse and neurodevelopment pathways in FCDII.

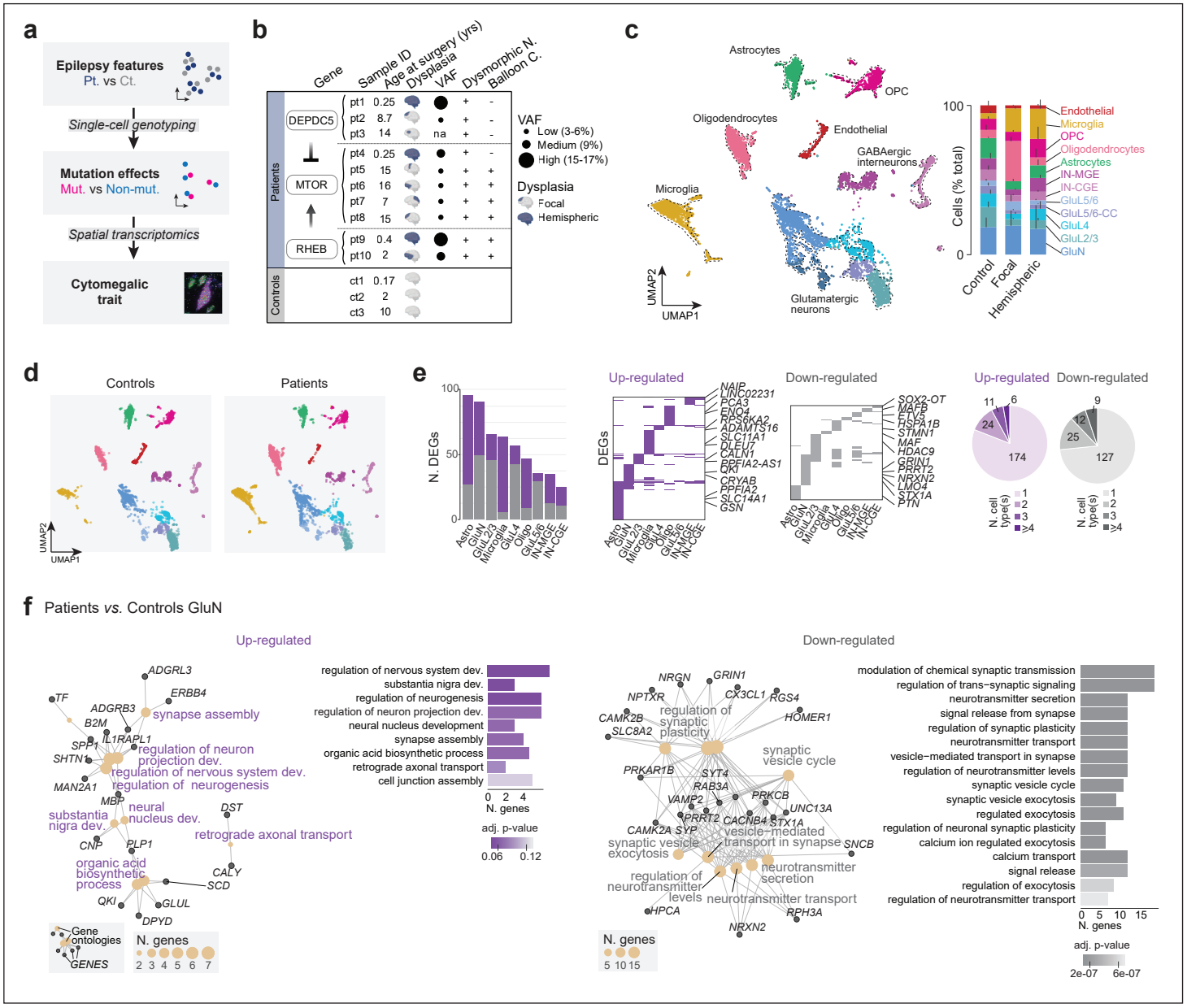

a, Workflow of the study. Single-nucleus RNA sequencing (snRNA-seq) was employed to examine transcriptional changes related to epilepsy in FCDII tissues. Genotypes of mutation sites were examined within patients' nuclei to compare mutated and non-mutated cell lineages. Integration of these findings with spatial transcriptomics of FCDII tissues allowed for the correlation of transcriptional alterations with cellular dysmorphology and spatial disorganization.

b, The subject cohort includes frozen brain tissues from ten patients (pt1-10) and three postmortem age-matched neurotypical controls (ct1-3). Dysplastic areas in pt1, 4, and 9 extended to an entire hemisphere, with pt4 and 9 diagnosed with hemimegalencephaly. “VAF” refers to the variant allele frequency of somatic mutations for each patient; na: not available (no somatic hit identified); yrs: years. Plus or minus signs indicate the presence or absence of dysmorphic neurons and balloon cells. Abbreviations: N., neurons; C., cells.

c, Left: UMAP dimensionality reduction of integrated snRNA-seq data of patients and controls using previously published age-matched control nuclei[22]. Cell-type annotations were adapted from a prior study[22] (see methods). Dashed lines outline cluster densities. Right: Cell type proportions in controls and patients with focal or hemispheric dysplasia. Abbreviations: Glu, glutamatergic; N, neurons; L, layer; CC, cortico-cortical projection neurons; IN-MGE, interneurons originating from the medial ganglionic eminence; IN-CGE, interneurons originating from the caudal ganglionic eminence; OPC, oligodendrocyte precursor cells.

d, UMAP visualization showing control and patient nuclei. Outlines of cluster densities are represented with dash lines.

e, Cell-type-specific differential gene expression (DEG) analysis between patients with focal FCDII and controls. Left: Number of DEGs per cell type (DEGs; significant genes expressed in at least 25% of cells with absolute log2 fold change > 0.4). Middle: Specific and shared DEGs across cell types; examples of DEGs specific to one cell type are indicated. Right: Proportion of DEGs specific to one or more cell types.

f, Top gene ontologies (GO) and associated genes for GluN differentially expressed genes.

Fig. 2 | Mutated cells are predominantly glutamatergic neurons and exhibit only occasional cytomegalic phenotypes.

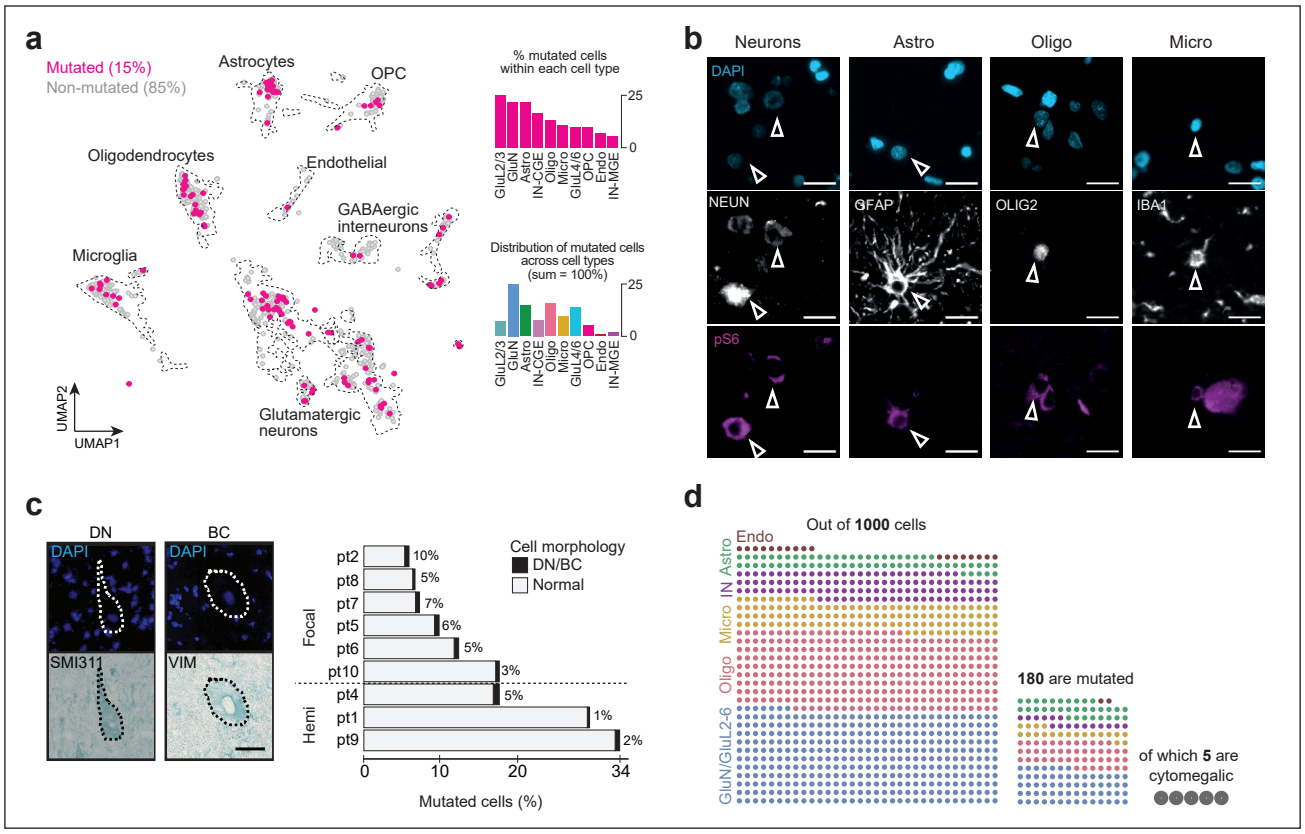

a, Mutation-positive nuclei are distributed across various cell types in the UMAP space with an enrichment observed in glutamatergic neurons and astrocytes. Right: percentage of mutated nuclei per cell type (top) and percentage of mutated nuclei across cell types (bottom). Abbreviations: GluN, glutamatergic neurons; GluL2/3, glutamatergic neurons of layers 2 and 3; GluL4/6, glutamatergic neurons of layers 4 to 6; IN-MGE, interneurons originating from the medial ganglionic eminence; IN-CGE, interneurons originating from the caudal ganglionic eminence; Astro, astrocytes; Oligo, oligodendrocytes; OPC, oligodendrocyte precursor cells; Micro, microglia; Endo, endothelial cells.
b, Representative images of co-immunofluorescence staining on FFPE sections using pS6 to label mTOR-hyperactive neurons (NeuN+, pt2), astrocytes (GFAP+, pt2), oligodendrocytes (OLIG2+, pt2) and microglia (IBA1+, pt10). Nuclei (in blue) are labeled with DAPI. Scale bars = 20µm.
c, A minor fraction of FCDII mutated cells exhibit cytomegalic features. Left: representative immunostaining of SMI311+ dysmorphic neuron (DN) and VIM+ balloon cell (BC) on frozen brain tissue from pt5, nuclei (in blue) are labeled with DAPI for total cell counting. Scale bar = 25µm. Right: percentage of mutated cells (inferred by the detected VAF) and proportion of DN/BC identified in each patient. Abbreviations: Hemi, hemispheric.
d, Representative schematic of the distribution of mutated cells across cell types and the fraction of mutated cytomegalic cells in pt10.

Fig. 3 | Cell-type-specific transcriptional dysregulation in FCDII mutated cells.

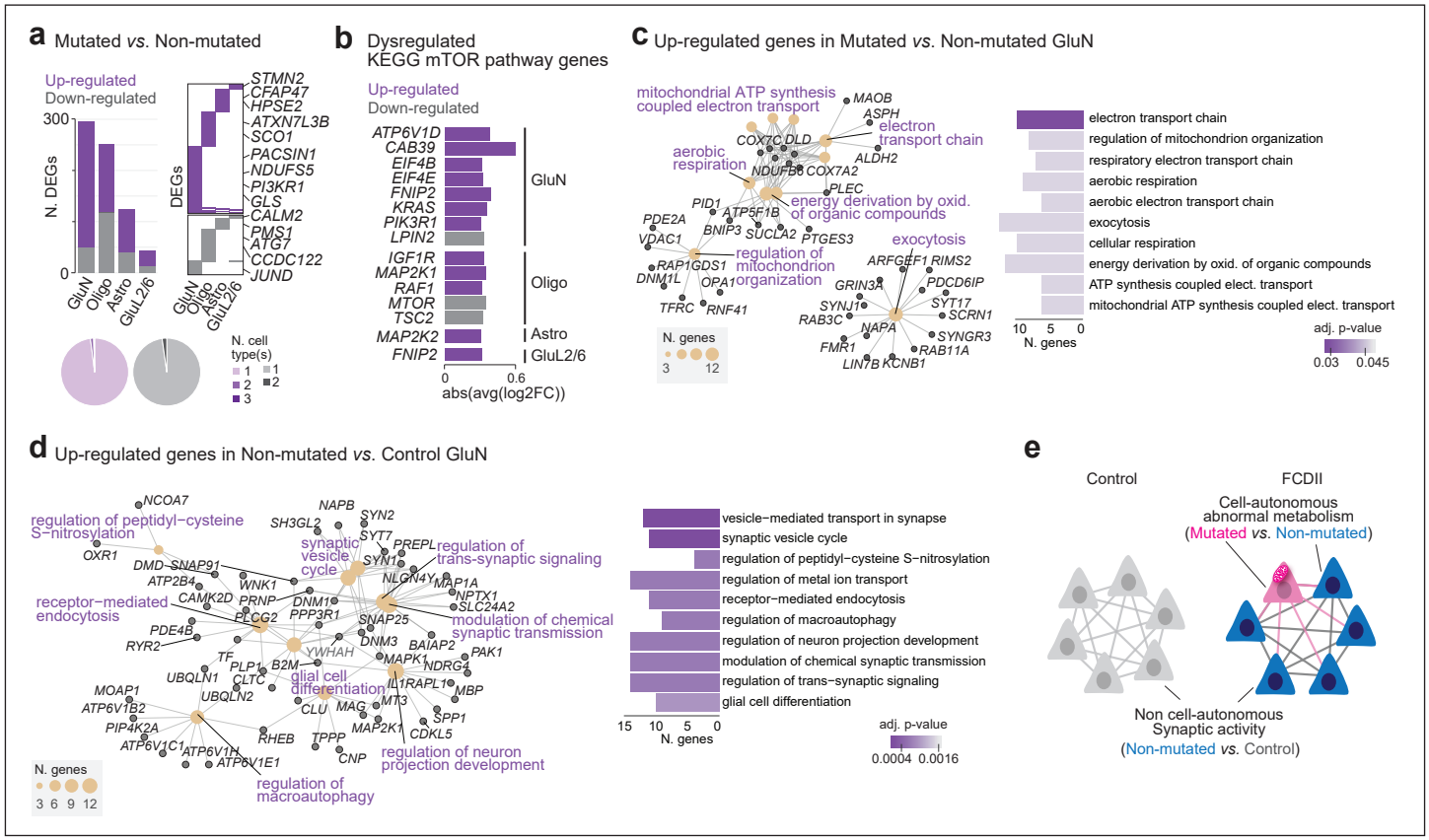

a, Cell-type-specific differential gene expression analysis between mutated and non-mutated nuclei from patients. Top Left: Number of differentially expressed genes (DEGs) per cell type (significant genes expressed in 25% of cells with absolute logarithmic fold change (logFC) > 0.3). Top right: Specific and shared DEGs across cell types; examples of DEGs specific to one cell type are indicated. Bottom: Proportion of DEGs specific to one or more cell types.
b, Absolute average logarithmic fold change (logFC) values for DEGs belonging to the mTOR signaling pathway from the KEGG database across cell types.
c-d, Top gene ontologies (based on adjusted (adj.) p-values) with corresponding genes for up-regulated DEGs in mutated vs. non-mutated GluN (c) and in non-mutated vs. control GluN (d). Similar ontologies were grouped into one single term.
e, Schematic of cell-autonomous metabolic alterations and non-cell-autonomous synaptic activity changes in FCDII.

Fig. 4 | Dysmorphic neurons and balloon cells belong to glutamatergic and astroglial lineages and display metabolic dysregulations.

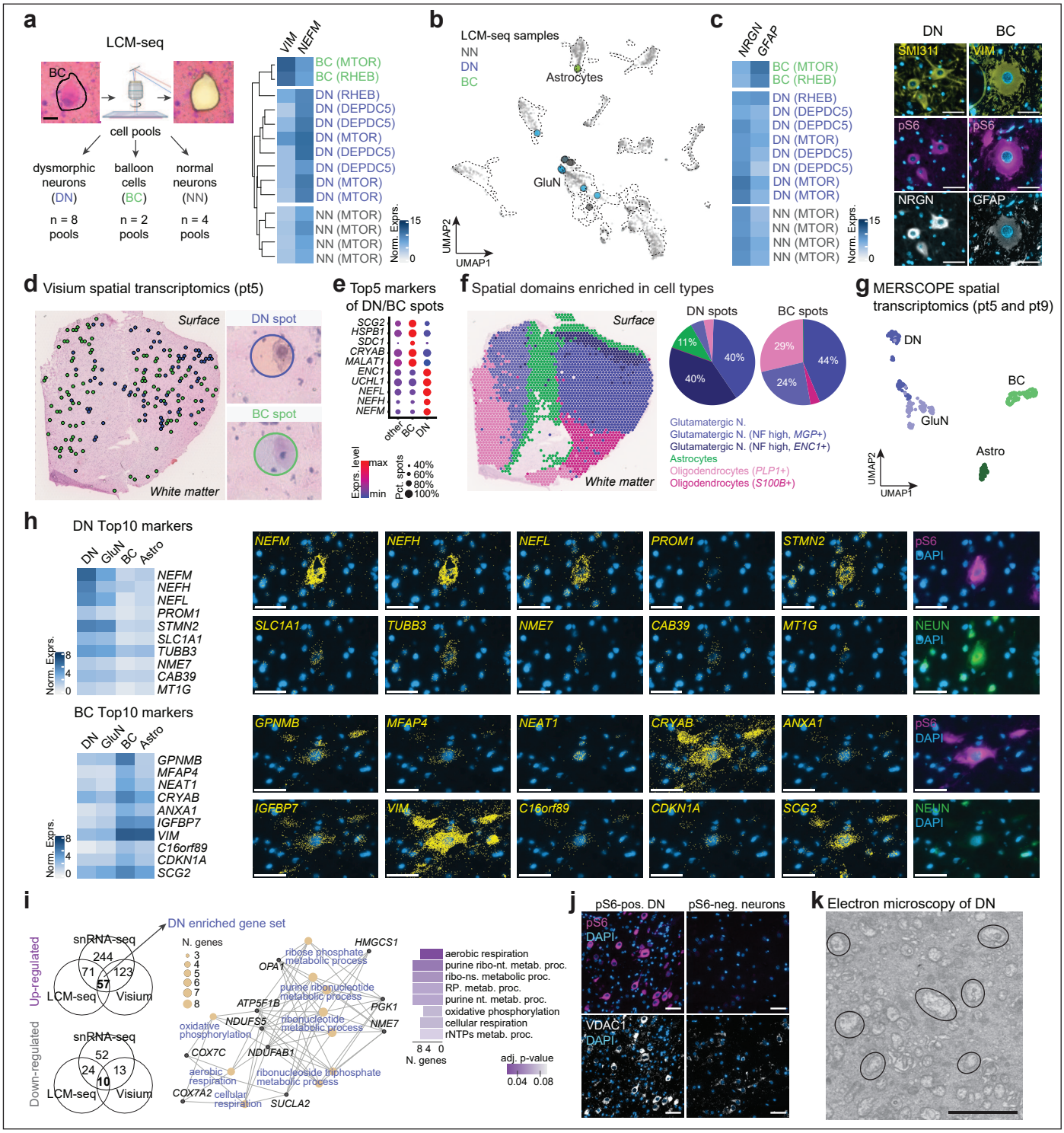

a, Left: LCM-seq workflow for dissecting and sequencing pools of DN, BC and NN from 8 patients. Right: heatmap of VST normalized average gene expression of DN and BC marker genes NEFM and VIM, and unsupervised hierarchical clustering of LCM-seq samples. **b,** Label transfer of LCM-seq samples in the snRNA-seq UMAP space. NN and DN match with GluN, and BC with astrocytes. **c,** Left: heatmap of VST normalized average gene expression of NRGN and GFAP, markers of GluN and astrocytes, respectively. Right: Co-immunofluorescence staining showing NRGN protein in pS6-SMI311 double-positive DN, and GFAP in pS6-VIM double-positive BC in pt5. GFAP-pS6 and VIM-pS6 double-stainings were performed on two consecutive sections and the same BC was recognized in both sections. Nuclei (in blue) are labeled with DAPI. Scale bar = 50µm. **d,** Visium spatial transcriptomics: spots containing DN and BC are intermingled across the tissue in pt5. Magnified images of representative DN- and BC-containing spots after HE staining are provided. **e,** Top markers of DN- and BC-containing spots in pt5. Known histological markers for DN (NEFM) and BC (CRYAB) are enriched in spots with DN and BC. **f,** Spatial semi-supervised clustering of Visium spots from pt5 shows clusters enriched in glutamatergic neurons, astrocytes and oligodendrocytes. Genes in parentheses indicate the top markers of the clusters. **g,** MERSCOPE analysis of manually selected single cells from pt5 and pt9. Separate clusters for DN, BC, astrocytes (Astro) and GluN are identified in the UMAP space. **h,** Heatmap of the SCTransform normalized average expression of the top 10 marker genes of DN and BC across pt5 and pt9 MERSCOPE data. Representative MERSCOPE images of these markers in DN and BC from pt5 are shown. DN are identified as pS6-NeuN double-positive; BC as pS6-positive and NeuN-negative. Scale bar = 50µm. **i,** Left: Number of GluN genes (dysregulated in mutated vs. non-mutated GluN nuclei from snRNA-seq) validated in DN by LCM-seq and Visium. Right: Top gene ontologies of DN up-regulated genes. **j,** Representative images of co-immunofluorescence staining of VDAC1 and pS6 proteins in pt2. Strong VDAC1 signal is detected in DN. Scale bar = 50µm. **k,** Electron microscopy of DN from pt5 shows accumulation of vesicular-swollen damaged mitochondria (black circles). Scale bar = 2.5µm

Supplementary Files

This is a list of supplementary files associated with this preprint. Click to download.

- 10xFCD2ExtendedDataFigures.pdf
- 10xFCD2InventorySupportingInformation.pdf